# Extracellular filaments revealed by affinity capture cryo-electron tomography of lymphocytes

**Leeya Engel**[1, 2, ✉], **Magda Zaoralová**[3], **Momei Zhou**[4], **Alexander R. Dunn**[1], **and Stefan L. Oliver**[4,✉]

[1]Department of Chemical Engineering, Stanford University, Stanford, CA, USA 94305
[2]Faculty of Mechanical Engineering, Technion - Israel Institute of Technology, Haifa, Israel 3200003
[3]Department of Molecular and Cellular Physiology, Stanford University School of Medicine, Stanford, CA, USA 94305
[4]Department of Pediatrics, Division of Infectious Diseases, Stanford School of Medicine, Biomedical Innovations 240 Pasteur Drive, Stanford, CA, USA 94305

**Cryogenic-electron tomography (cryo-ET) has provided an unprecedented glimpse into the nanoscale architecture of cells by combining cryogenic preservation of biological structures with electron tomography. Micropatterning of extracellular matrix proteins is increasingly used as a method to prepare adherent cell types for cryo-ET as it promotes optimal positioning of cells and subcellular regions of interest for vitrification, cryo-focused ion beam (cryo-FIB) milling, and data acquisition. Here we demonstrate a micropatterning workflow for capturing minimally adherent cell types, human T-cells and Jurkat cells, for cryo-FIB and cryo-ET. Our affinity capture system facilitated the nanoscale imaging of Jurkat cells, revealing extracellular filamentous structures. It improved workflow efficiency by consistently producing grids with a sufficient number of well-positioned cells for an entire cryo-FIB session. Affinity capture can be extended to facilitate high resolution imaging of other adherent and non-adherent cell types with cryo-ET.**

**cryo-EM | cryo-ET | Jurkat cells | micropatterning | lymphocytes**
**Correspondence:** ***sloliver@stanford.edu, leeya@technion.ac.il***

## Introduction

Cryogenic-electron tomography (cryo-ET) is a state-of-the-art electron microscopy (EM) modality used for the structural analysis of intact, vitrified cells at the nanometer and subnanometer scales (1–6). In preparation for cryo-ET, cells are deposited or grown on specialized substrates called EM grids. To image eukaryotic cells, which are on the length scale of micrometers, thinning the cells using techniques such as cryo-focused ion beam (cryo-FIB) milling is typically required. Cells often to distribute in a nonuniform manner on EM grids, and settle on the metal grid bars where they are not accessible for cryo-FIB and cryo-ET. In addition, cells can form clumps that prevent proper vitrification and successful FIB milling. These limitations present an obstacle both to the collection of cryo-ET data of sufficient quality from biological specimens and to the automation of data collection and cryo-FIB milling.

To gather sufficient data for high resolution structural determination, reproducible samples are needed. Time on high-end cryo-FIB and cryo-ET instrumentation, typically accessed through shared cryo-EM facilities, is expensive and limited. An ideal sample for cryo-FIB/cryo-ET would have a repeatable and uniform distribution of cells situated in the centers of the grid squares. We and others have published studies demonstrating the positioning of individual adherent cells (7–11) or adherent cell pairs (12, 13) on EM grids micropatterned with extracellular matrix (ECM) proteins in preparation for cryo-ET. Another approach for providing a uniform distribution of cells for cryo-FIB/cryo-ET, applicable to both adherent and non-adherent cell types, is the Waffle Method (14). It employs high pressure freezing to vitrify a contained, continuous suspension of cells in preparation for cryo-FIB/cryo-ET. High pressure freezing, however, can be technically challenging and results in thicker samples (10s of microns) that require extended cryo-FIB milling times.

Lymphocytes (e.g., T-cells and B-cells) are minimally adherent cells that play important roles in the body's defense against infectious diseases and cancer. Recent advances in our understanding of lymphocyte function have been provided by fluorescence imaging and conventional EM (15, 16). However, the resolution of fluorescence imaging is limited by the wavelength of light and conventional EM techniques require fixation and staining steps that can distort or destroy delicate biological structures.

Here we present an affinity capture system that facilitates high throughput cryo-FIB milling and subsequent nanoscale imaging by cryo-ET of non-adherent cell types that is compatible with vitrification by plunge-freezing. We micropatterned antibodies (Abs) on EM grids to capture T-cells as well as Jurkat cells, an immortalized line of human T lymphocytes, and position them in the centers of EM grid squares. This facilitated our observation of nanoscale filaments emanating from the Jurkat cells. Subtomogram averaging (STA), RNA-seq, and flow cytometry identify these structures as intermediate filaments composed of vimentin. To our knowledge, this is the first time that micropatterning has been used to prepare minimally adherent cell types for cryo-ET.

## Results

To assess the feasibility of capturing non-adherent cell lines on EM grids, a T-cell specific antibody to human CD3 (epsilon chain) was micropatterned to trap the T-cell surrogate, Jurkat cells, on islands within grid squares. Affinity capture grids were able to successfully capture single Jurkat cells and position them in the centers of the grid squares (Figs. 1A-C,

S1, S2). Cell localization was restricted to the micropatterned region on EM grids treated with the anti-CD3 antibody (Fig. 1B and 1C). Neither of the control conditions, micropatterned grids without Ab or with a nonspecific Ab (gE), contained cells following a rinse (Fig. S1). We were also able to use this workflow to capture and position primary T-cells on EM grids micropatterned with anti-CD3 islands (Fig. S3).

The number of Jurkat cells occupying a given grid square increased with the size of the micropatterned Ab island (Fig. 2). Micropatterned islands that were about half the size of Jurkat cells (i.e., 5 µm) were unable to capture the cells. Circular 10 µm islands of micropatterned anti-CD3 were ideal for vitrification and cryo-FIB/SEM of Jurkat cells (Fig. 1C-F). A typical affinity grid seeded with Jurkat cells contained more well-positioned single cells than can be milled in a typical manual cryo-FIB session (>10) (Fig. 1C, D). The target thickness (175 nm) of individually cryo-FIB milled Jurkat cells was readily achieved (Fig. 1E, F).

Cryo-ET of the cryo-FIB milled lamellae revealed cellular features within and external to the Jurkat cells (Figs. 3, 4, 5, S4). Jurkat cells are designated as a T lymphoblast. Their morphology, which comprises a large nucleus with very limited cytoplasm, was apparent in the montage images captured by cryo-TEM (8,700x magnification) of the lamellae (Fig. 4). While Jurkat cells had a smooth and round appearance when observed with light microscopy and cryo-SEM (Figs. 1, 2, and 3), extracellular, filamentous structures were revealed at the periphery of the cells in the tomograms reconstructed from the cryo-ET tiltseries (Figs. 3, 4, 5, and movies 1 and 2). The filaments were observed only at the trailing edge of lamellae, which captures the interface between the Jurkat cell and the $SiO_2$ surface of the micropatterned grid (Fig. 4, Table S1). They appear to emanate from the plasma membrane of the cells.

Within the reconstructed tomograms, the dimensions of the filaments were determined to have an external diameter of approximately 10 nm and an apparent internal diameter of approximately 3 nm, bringing them into the range of intermediate filaments (Fig. S5). Based on electron density, the filaments appeared to be hollow. Although the length of the filaments could not be determined from the cryo-tomograms, they are likely on the order of micrometers as they traverse the entire field of view of the tilt series and can be seen forming an extensive net-like structure in the medium magnification montages (Fig. 4 and Fig. 3C). Although the extracellular filaments appeared to form quasi-random networks close to the cell surface, they also appeared to form membranous bundles of 2-7 filaments, in particular in the regions between contacting cells (Fig. 5A, B and Table S2). The shorter distance between the filaments in the bundles between cells (8.6 nm [0.124]) compared to filaments in bundles open to the extracellular environment (12.49 nm [0.622]), suggests that the structures are compressible (Table S2). Segmentation of the cryo-tomograms also revealed the nuclear envelope, vesicular structures, and plasma membrane (Fig. 5B,D).

The abundance of filaments within the cryo-tomograms allowed for the reconstruction of an 8.4 Angstrom cryo-EM map (Fig. 6). The architecture of the approximately 10 nm intermediate filaments suggested a parallel arrangement of proteins with long, bundled alpha-helices as the map density had a larger volume than a single alpha helix (Fig. 6A). End-on views of the cryo-EM map revealed either 3 or 4 repetitive units. (Fig. 6B). The map density also revealed potential sites of inter helical bundle connections. Each of these features is indicative of intermediate filaments, which are composed of proteins with a central alpha-helical rod domain and a variable head and tail that form coiled-coiled dimers (17). This suggested that the filaments were composed of tetramers or dimers.

Because the resolution of the cryo-EM map was not sufficient to identify the constituent proteins of the filaments, RNA sequencing was performed to determine the levels of transcription from intermediate filament genes of Jurkat cells and control human embryonic lung fibroblasts (HELFs). Of the 71 genes associated with intermediate filament proteins only two type I/II (KRT1 and KRT10) and one type III (VIM) were abundantly expressed (>100 normalized reads) intermediate filament genes compared to eight type I/II/III for the HELF controls (Table S3). Vimentin (VIM) was detected on the external surface of Jurkats cells by flow cytometery of non-permeabilised (surface) and permeabilised (total) cells (Fig. S7 and S8). Compared to no antibody or isotype controls, vimentin was detected in almost all (>98%) permeablised and non-permeablised Jurkat cells. The levels of total and cell surface vimentin were not altered by incubating Jurkat cells with an isotype control, anti-CD4 or anti-CD3 antibodies prior to fixation. These data strongly support the notion that the extracellular filaments observed by cryo-ET are vimentin intermediate filaments.

## Discussion

We have demonstrated an affinity capture system for positioning lymphocytes for cryo-FIB milling and cryo-ET. T-cells have been observed in the literature to form stable attachments to micropatterned islands of CD3 antibodies on glass surfaces (18), which is likely the mechanism underlying affinity capture on EM grids.

Affinity capture grids facilitated our observation of nanoscale filaments on the surface of Jurkat cells (Figs. 3,5,4). The dimension of the filaments measured from our tomography data (10 nm, Fig. S5) was uniform and consistent with intermediate filaments, such as keratin, recently observed in the extracellular space (19, 20). The glycocalex is known to have a filamentous architecture, but in contrast to the filamentous network we observed, it is heavily interconnected with a wide distribution of filament diameters (3-15 nm) (21, 22). The long helical structures seen in the 8.4 Angstrom cryo-EM map (Fig. 6) together with the high levels of expression seen in the RNA sequencing (Figs. S7-S11), strongly support vimentin as the major constituent of the filamentous networks observed in the Jurkat cell extracellular space. Intracellular vimentin intermediate filaments are known to provide structural support to lymphocytes (23–25), but vimentin also plays crucial roles in lymphocyte migration and attachment

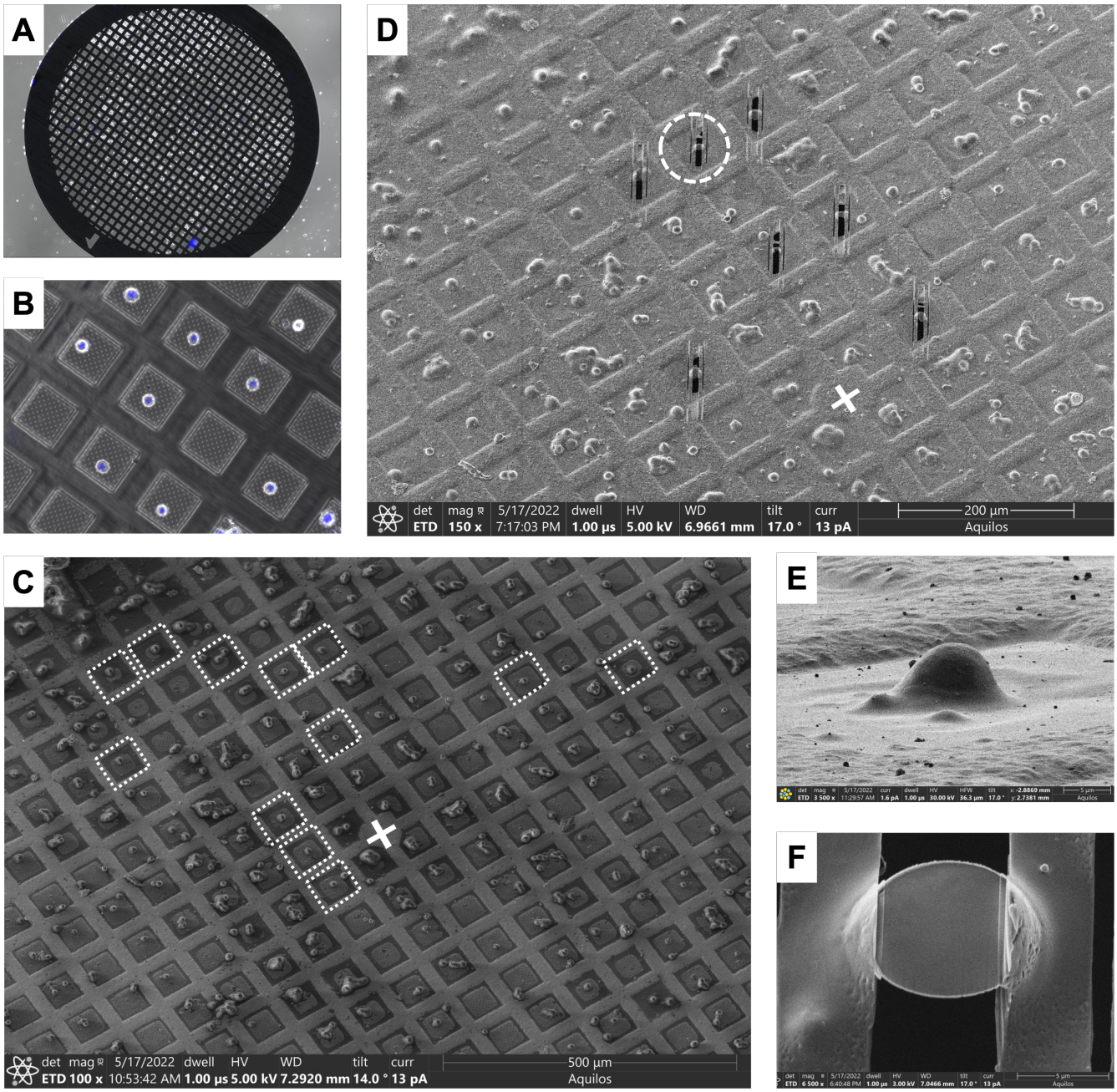


**Fig. 1.** Affinity capture EM grids facilitate cryo-FIB of minimally adherent cells. (A) Fluorescence image overlaid with brightfield image of 300 mesh EM grid micropatterned with 10 µm circles following antibody incubation and cell capture. (B) Close up shows single cells centrally positioned on grid squares (nuclei are in blue). (C) Cryo-SEM image of an EM grid with vitrified cells centrally positioned in grid squares suitable for cryo-FIB (denoted by dotted white squares). The grid center is marked with a white cross. (D) Cryo-SEM image of the EM grid from C after cryo-FIB milling of seven Jurkat cells, with the grid center marked with a white cross. As is typical for cryo-FIB, all milled cells are north of the grid center. (E) Ion beam image of a platinum-coated Jurkat cell selected for cryo-FIB milling, indicated in D by the white dotted circle. (F) The lamella generated from the cell in E by cryo-FIB milling.

to the vascular endothelium (26, 27). For example, vimentin deficient lymphocytes demonstrated reduced adhesion to endothelial cells and collagen (27, 28). Recent studies revealing vimentin on the plasma membrane surface or in the extracellular space of different cell types and in different physiological and pathological conditions have been reviewed by Paulin et al. (29). The role of extracellular/cell surface vimentin, how it is secreted from the cell, and what domains of vimentin are expressed on the surfaces of different cell types (e.g., lymphocytes vs. endothelial cells) are are still being explored (29–31). It is also unclear whether fixation, as performed in this study prior to plunge-freezing, influences extracellular vimentin.

Vimentin monomers assemble into parallel homodimers that form higher order structures of anti-parallel adjacent dimers aligned exclusively in an approximately half-staggered anti-parallel A11 mode with a distance of 3.2–3.4 nm between their axes (17). The cryo-EM map of the intermediate filaments is highly suggestive of such a higher order vimentin complex given the long alpha helical-like densities that have

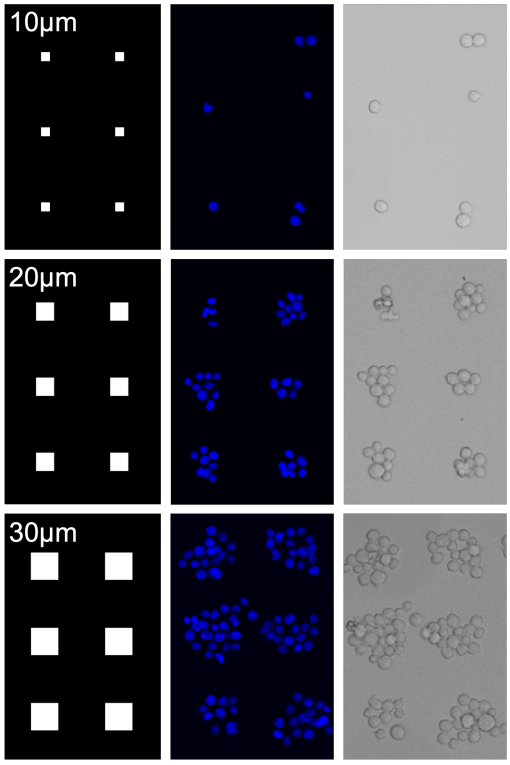


**Fig. 2.** Cell occupancy increases with larger micropatterned anti-CD3 islands. Examples of micropatterned squares with side lengths ranging from from 10 µm to 30 µm. Left panel: digital micropatterns designed to match the pitch of a 300 mesh EM grid. Jurkat cells attached to micropatterned glass incubated with an anti-CD3 mAb. DAPI (middle panel), brightfield (right panel).

connecting densities. A recent study of mouse embryonic fibroblasts demonstrated that intracellular vimentin intermediate filaments assembled into higher order structures, a helical assembly of 5 spring-like protofibrils, compared to the proposed tetramer of dimers for the extracellular filaments from Jurkat cells in the present study (32). The differences in these higher order architectures suggest that the role of vimentin intermediate filaments is context specific and cell type dependent. Furthermore, it remains unclear how these long, apparently membrane-less projections, emerge from the cell. To the best of our knowledge, this is the first time networks of intermediate filaments have been observed at the nanoscale in the extracellular space. Jurkat cells have been observed to shed microvillus membrane particles on anti-CD3 treated surfaces using total internal reflection fluorescence microscopy (TIRF) (16), but the filaments that appear in our cryo-tomograms (Figs. 3C and 4D) are too small (10 nm) to be observed by fluorescence microscopy. The filaments were also not observed by conventional transmission and scanning EM (TEM and SEM) imaging of the Jurkat cell surface (16). While these EM modalities can provide higher resolution than light microscopy, in contrast to *in situ* cryo-ET, they require preparation steps that would likely cause the collapse of delicate structures such as networks of filaments on the cell surface. Specifically, for conventional SEM of cells, preparation steps include fixation, dehydration, and the deposition of a conductive metal layer. For conventional TEM, preparation of cells includes fixation, dehydration, resin embedding, staining, and sectioning. Cryo-ET overcomes the limitations of these destructive processing methods, providing the highest resolution imaging of cells preserved in a hydrated, near-native state. Cryo-FIB allows for the generation of nearly distortion-free thin sections of vitrified cells (33–35). In our cryo-FIB/cryo-ET study, preservation of nanoscale biological structures through vitrification converged with three-dimensional image processing techniques to provide an unprecendented view of the nanoscale environment of the Jurkat cell surface. Other recent studies have demonstrated the power of the cryo-FIB/cryo-ET platform to reveal additional complexity to biological structures such as microvilli despite decades of structural analysis by conventional EM (36).

The affinity capture system improves sample usability, reducing the cost and preparation time required to prepare cellular samples for cryo-FIB/cryo-ET. Beyond positioning cells and limiting the number of cells that attach to a given region of the substrate, the use of micropatterned islands functionalized with antibodies, ligands, and ECM proteins can potentially be extended to select for and capture cell types of interest from diverse cell populations. Alternatively, two different antibodies can potentially be patterned to capture different cell types within the same grid square for co-culture studies. We envision the workflow presented here facilitating future analysis of the nanoscale structures involved in T-cell activation. Patterns comprised of different ligands can potentially be used to study how the spatial organization of signaling complexes impacts the structures involved in cell communication (18), such as receptor arrangement (37). An extension of this idea is to facilitate studies of the nanoscale architectures involved in signaling events or the growth and structure of nanoscale bridges (i.e., tunneling nanotubes) by using micropatterning to control the distance between captured cells (38, 39).

Appropriately packaged affinity capture EM grids could assist non-experts (e.g., clinicians lacking EM experience) with preparing and shipping clinically-relevant cells to cryo-EM facilities for cryo-ET imaging. Packaging methods currently include the use of 3D printed grid holders (40) and silicone wells in glass-bottom dishes that exploit the surface tension of liquid droplets contained to the wells to immobilize EM grids (11). Devising storage methods that increase the shelf life of micropatterned EM grids is an important future area of research toward increasing access to affinity capture EM grids.

## Methods

**EM Grid Micropatterning.** To accommodate single Jurkat cells, we micropatterned squares and circles varying from 5 to 30 µm across on 300 mesh gold grids coated with a thin perforated layer of silicon dioxide (Quantifoil R1/4). The grids were exposed to atmospheric plasma, incubated in poly-l-lysine (PLL, Sigma cat # p4707), incubated in mPEG-Succinimidyl Valerate, MW 5,000 (PEG-SVA, Laysan Bio Inc) and then UV exposed according to digitally generated micropatterns using the Primo photo-micropatterning system

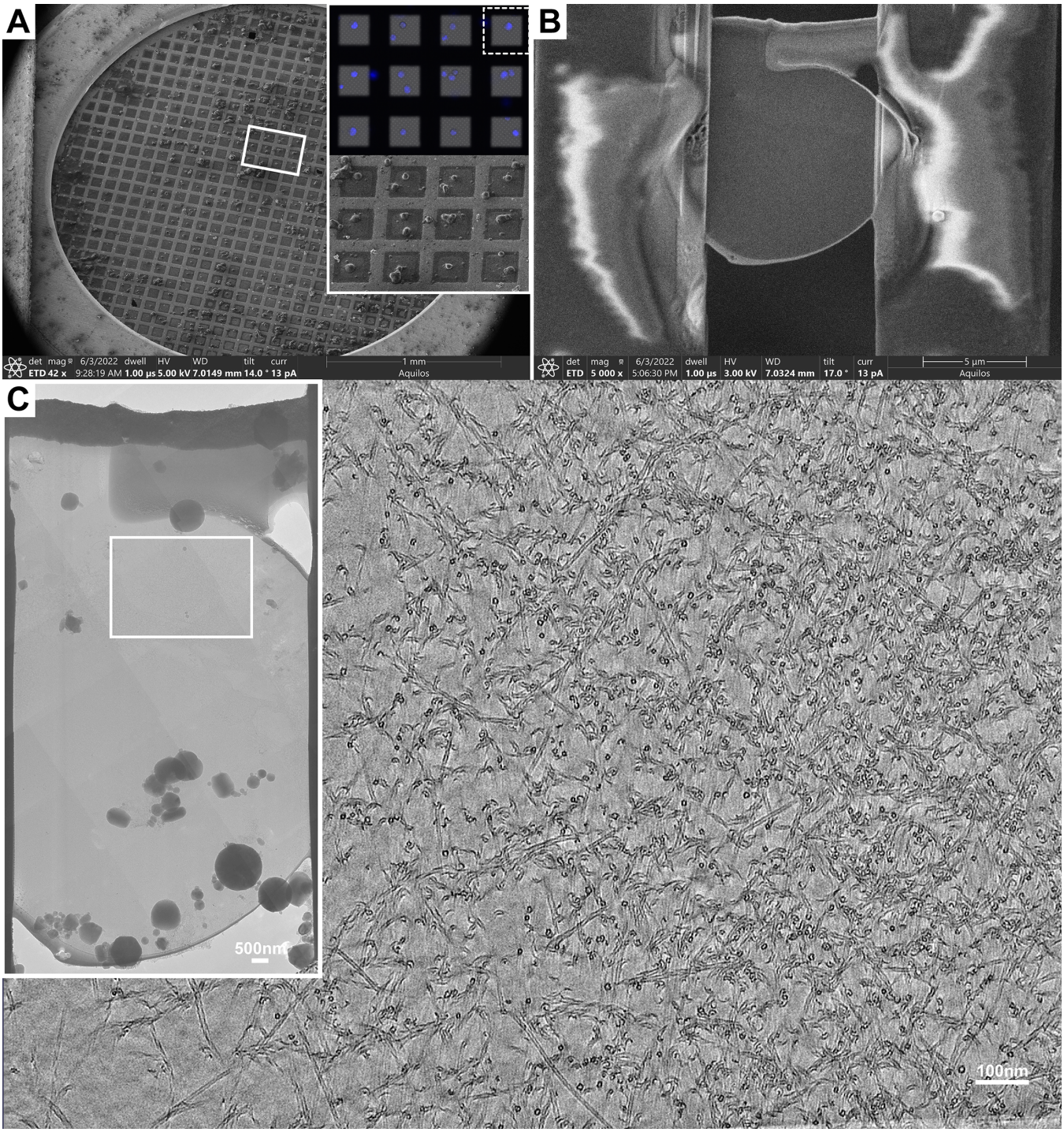


**Fig. 3.** Cryo-FIB/cryo-ET identifies filaments emanating from Jurkat cells on affinity captured grids. (A) Cryo-SEM of cells vitrified on an affinity capture grid micropatterned with 10 µm circles. Inset shows live-cell fluorescence micrograph of nuclei stained with Hoechst 33342 as well as a close up on the SEM image. (B) A lamella produced from a Jurkat cell via cryo-FIB milling with an Aquilos2. The lamella was produced from the cell highlighted by the dotted box of the inset in panel A. (C) Cryo-ET of the lamella from panel B. The inset shows a medium magnification (8,700X) montage of the lamella. The white box highlights the area where a tilt series was collected to produce a cryo-tomogram; a single slice is shown (see Suppl. Movie 1 for the entire tomogram).

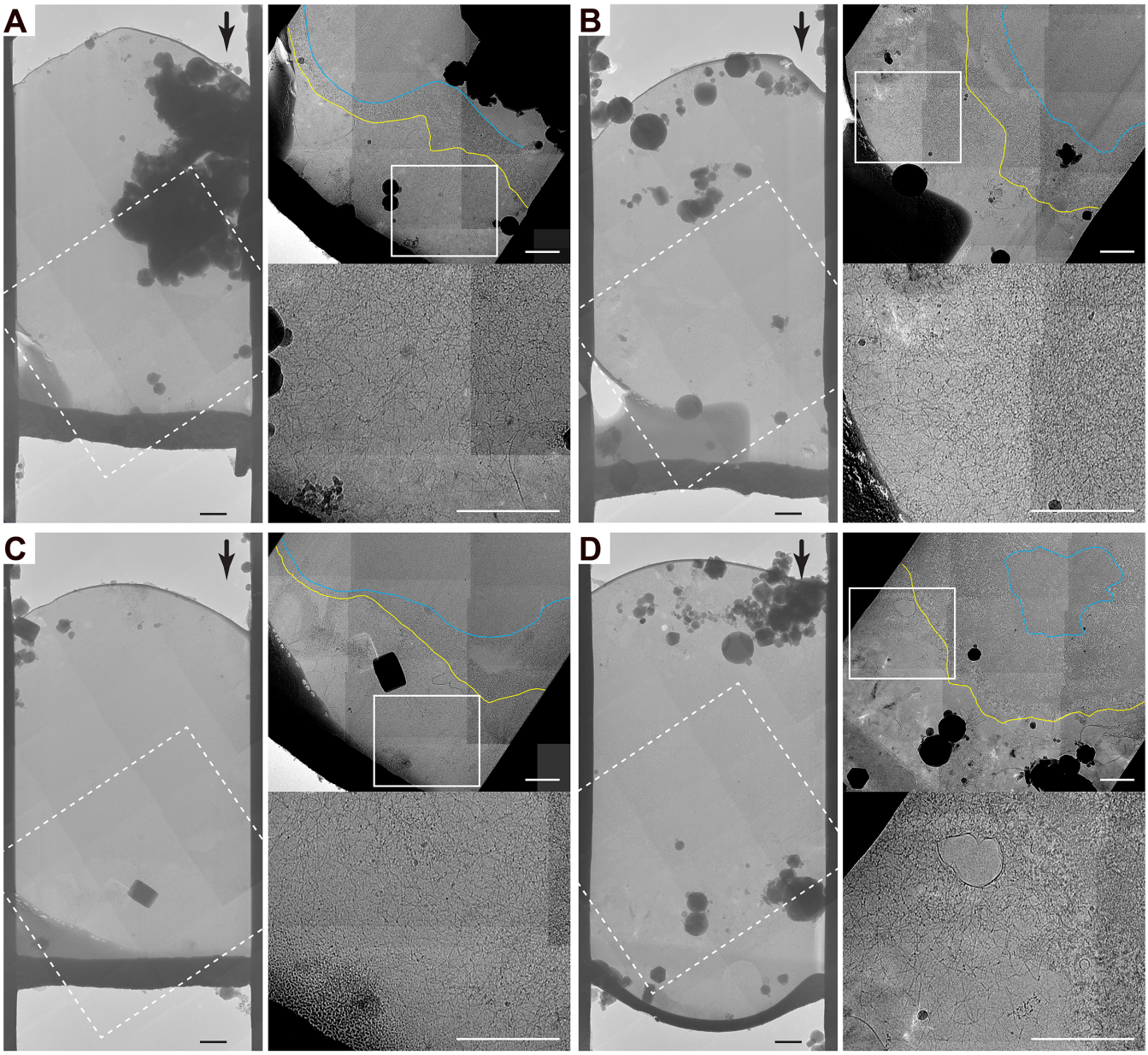


**Fig. 4.** Jurkat cell extracellular filaments were localized at the $SiO_2$ substrate-cell interface. (A-D) Four examples of cryo-TEM montages (8,700x; 20Å/pixel) of lamellae cryo-FIB milled from micropatterned Jurkat cells. The black arrow in each left hand panel points to the thin layer of platinum coating the top of the cell and indicates the direction of cryo-FIB milling. The region wherethe thicker dark band below the cell meets the lighter gray region is the $SiO_2$-Jurkat cell interface. The dotted white boxes highlight the areas shown zoomed-in in the top right image of the panel. The blue lines represent the outline of the nuclear envelopes, the yellow lines represent the outline of the plasma membrane, and the white box highlights the zoomed in area in the lower right panel revealing the intermediate filaments. The contrast for the two right hand panels in A to D was adjusted to improve visibility of the filaments. All scale bars, 1000 nm.

(Alveole) to selectively degrade the PEG coating on the EM grids. A detailed protocol for micropatterning EM grids using this method has been made publicly available by the authors on the protocol sharing platform protocols.io (11).

Following micropatterning of the grids and sterilization in 70% ethanol (see aforementioned protocol), the grids were incubated in human anti-CD3 (clone UCHT1; Biolegend Cat# 300402) antibody overnight. Control conditions included a set of micropattterned grids that were not incubated in antibody (No Ab) and another set of micropatterned grids that were treated with monoclonal antibodies to VZV glycoprotein E (gE; EMD Millipore Cat# MAB8612).

For T-cells, 200 mesh gold Quantifoil holey carbon R2,2 grids were micropatterned followed the same protocol, but with micropatterned circles that were 7.5 and 15 µm in diameter.

**Jurkat Cell Culture and Seeding.** Jurkat cells (Jurkat, Clone E6-1, ATCC) were maintained following manufacturer instructions. A volume of 10 µL of a $7x10^6$ cells/mL suspension was seeded on the micropatterned grids and allowed to settle for two hours. The grids were then transferred to fresh 35 mm dishes with 10 mm 1.5 cover glass (MatTek) and washed extensively with media (RPMI 1640 + 10% FBS + 1% pen/strep). The grids were then washed once with 2

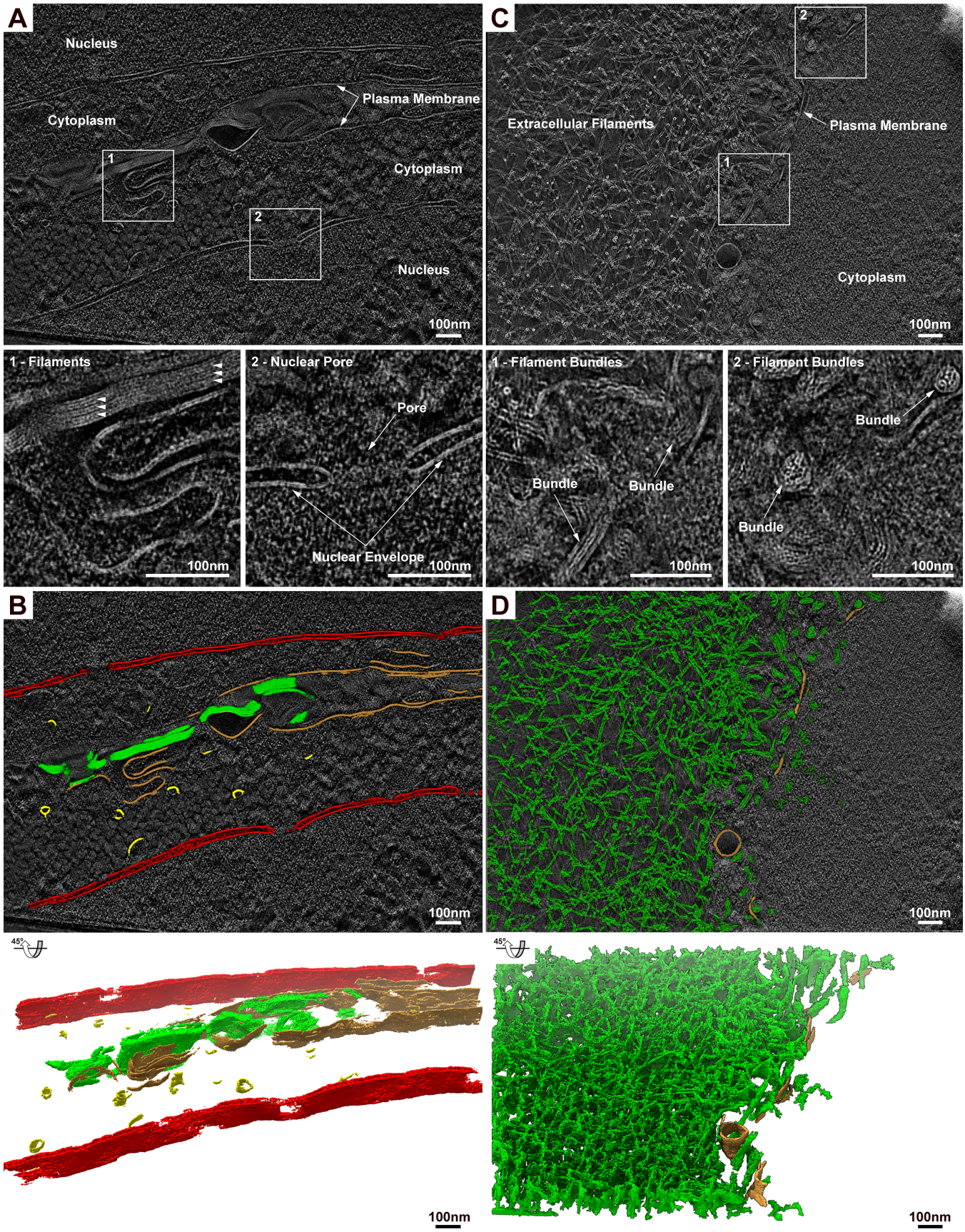


**Fig. 5.** Affinity capture grids facilitate the visualization of nanoscale structures at the plasma membrane of Jurkat cells via *in situ* cryo-ET. (A to D) Tomogram reconstructions and AI-based segmentation of cryo-FIB milled Jurkat cells. (A) Cryo-tomographic slice of the region between adjacent cells showing (1) bundled filaments and (2) a nuclear pore. (C) Cryo-tomographic slice showing extracellular filaments. In the region closer to the plasma membrane filament bundles can be seen from the side (1) and in cross section (2). (B and D) AI-based segmentation of filaments (green), plasma membrane (brown), vesicles (yellow), and nuclear envelope (red) identified in the tomograms for panels A and B. (See Suppl. Movie 2 for full tomograms and Figure S4 for lower magnification images of corresponding cells and lamellae.) All scale bars are 100 nm.

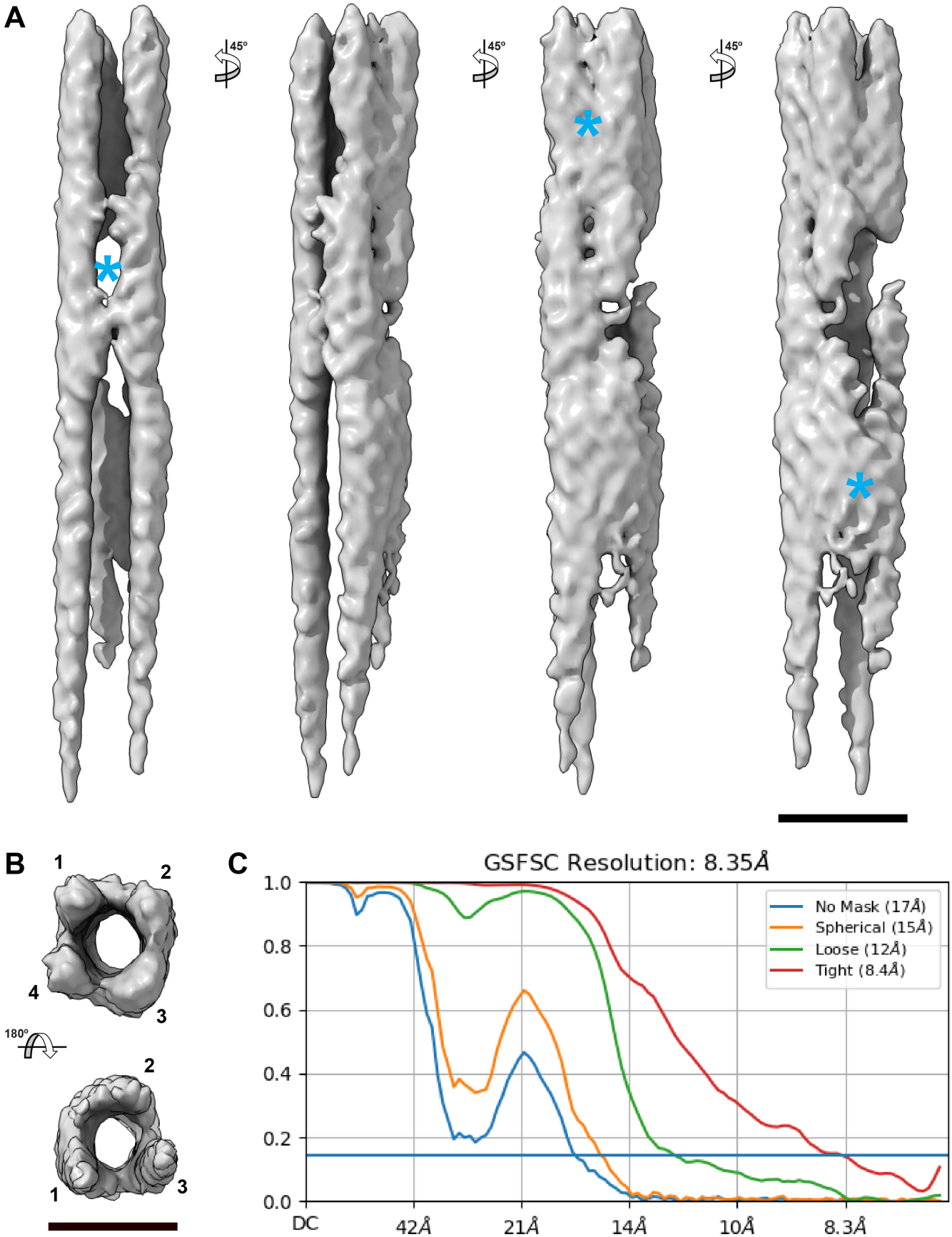


**Fig. 6.** Cryo-EM map of Jurkat cell extracellular intermediate filaments. (A and B) Side (A) and end-on (B) views of the cryo-EM map (8.4Å) of intermediate filaments reconstructed using cryoSPARC and viewed at 45° (A) and 180° (B) rotational intervals. The blue stars in A highlight regions of inter-filament contacts. The numbers in B represent the frequency of repetitive units visible at the end of the cryo-EM map. Scale bars, 100Å. (C) FSC curves generated by cryoSPARC for the cryo-EM map.

mL PBS, fixed in 1 mL 4% PFA, and washed twice with 2 mL PBS.
Prior to imaging, the PBS was aspirated and replaced with 2 mL PBS plus 1:1000 Hoechst 33342 to stain the cell nuclei. Images were captured with a BZ-X710 microscope (Keyence). Brightness and contrast in Fig. 2 were adjusted to improve visibility.

**T-cell Culture and Seeding.** Human T-cells (gift from Robbie Majzner's lab at Stanford University) were purified from isolated peripheral blood mononuclear cells as in Tousley et al. (41). They were maintained in AIM-V complete media (Gibco) supplemented with 5% FBS and IL-2 (2.18 IU/ng, Peprotech). To seed the cells on the micropatterned grids, 25 µL of a $4x10^5$ cell/mL suspension was added to each grid several times until we could observe approximately 2-3 cells above or on each grid square. Images of live T-cells on micropatterned Au 200 mesh holey carbon coated EM grids were captured after 5.5 hrs on an inverted Nikon Ti-E microscope (Nikon, Minato, Tokyo, Japan) equipped with a Heliophor light engine (89 North) and an Andor sCMOS Neo camera using a 20x Plan Apo Lambda air objective lens and a 60x Plan Apo Lambda oil objective lens. The samples were vitrified by plunge freezing.

**Vitrification and Cryo-FIB.** Samples were vitrified in a Leica EM GP plunge freezer and clipped into autogrids before being loaded into an Aquilos 2 (Thermo Fisher) for cryo-FIB milling. Lamella were cryo-FIB milled at a 10 degree milling angle first to a 5 µm thickness with a current of 1 nA. Microexpansion joints were cryo-FIB milled to prevent bending and breaking of the cryo-lamellae (42). Sequential milling was performed at 0.3 nA to 3 µm thickness, at 100 pA to 1µm thickness, and at 50 pA to 500 nm thickness. A final polish was performed with a 175 nm distance between rectangular patterns at a current of 30 pA.

**Cryo-ET Data Acquisition and Tomogram Reconstruction.** Samples were loaded into an FEI Krios G2 transmission electron microscope (TEM) equipped with a bioquantum energy filter and a K3 direct electron detector (Gatan). SerialEM software (43) was used to operate the TEM at 300 kV in low-dose mode and acquire tilt series at a magnification 26,000x (0.3366 nm/pixel). Tilt series were acquired with $2^o$ steps between -$60^o$ and +$60^o$ and a defocus of -4 µm. Additional data collection parameters are in Supplemental Table 4. Motion correction and tiltseries stack generation was performed with Warp software (44) and 3D reconstructions were calculated using the weighted-back projection using IMOD (45). AI segmentation of tomograms was performed using the Dragonfly (Version 2022.2.0.1367; Object Research Systems) Deep Learning Tool. UCSF Chimera was used for visualization of structures (46).

**Cryo-ET Map Reconstruction.** CryoSPARC was used to generate a reconstruction of the intermediate mediate filaments using the helical processing pipeline (Fig. S2). This approach was used due to the limited data acquisition for the intermediate filaments. Individual cryo-ET movie stacks with the accumulated dose information patch motion corrected and CTF estimation then used to manually pick 240 particles across 12 micrographs to generate a 2D class average for template picking. Iterative rounds of 2D classification, refinement, filament tracing were performed until cryo-EM map resolution could not be improved.

**RNA-seq of Jurkat Cells and HELFs.** Jurkat cells and HELFs were lysed with buffer RLT Plus following the manufacturer's instructions (Qiagen). RNA was purified from lysates using a RNeasy Plus Mini Kit (Qiagen). RNA-seq libraries and sequencing (RNA-seq) was performed by Medgenome. FASTQ files generated from the libraries were assessed and aligned to the human genome (hg19) using the STAR aligner in RNAdetector (47).

**Flow cytometry of Jurkat cells.** Jurkat cells were incubated with either CD4-FITC (clone: RPA-T4; Biolegend), CD3-FITC (clone: OKT3; Biolegend), or isotype-FITC (clone: MOPC-173; Biolegend) antibodies (1 µl per 2 x105 cells) or mock treated at 37 ºC for 1 hr then fixed with 4% paraformaldehyde. All samples were blocked with Human TruStain FcX (Fc Receptor Blocking Solution; Biolegend) on ice for 10 min before immunostaining with vimentin rabbit mAb conjugated with Alexa fluor 647 (clone: D21H3; Cell Signaling) or isotype control rabbit mAb conjugated with Alexa fluor 647 (clone: DA1E; Cell Signaling) on ice for 30 min, washed twice with ice-cold PBS (Gibco) supplemented with 0.5% BSA (Bovine serum albumin; Jackson ImmunoResearch) and 0.02% sodium azide (Sigma), then resuspended in ice-cold PBS supplemented with 2.5% FBS, 2 mM EDTA (Fisher scientific), and 0.2 µg/ml DAPI (Thermo Fisher Scientific). Stained cells were analyzed using Agilent Quanteon flow cytometer (Agilent), color compensation was performed using compensation beads (Biolegend) only, compensation beads with CD3-FITC antibody, compensation beads with vimentin Alexa fluor 647 antibody, and Live:Dead (1:1) with DAPI stain. Data were processed with FlowJo (TreeStar) to determine the percentage of live cells (DAPI signal), percentage of cells expressing vimentin (Alexa fluor 647 signal) and percentage of cells expressing CD4 or CD3 (FITC signal).

**ACKNOWLEDGEMENTS**

This work was supported by NIH R01 AI20459 (SO), R21 AI159375 (SO), R35 GM130332 (ARD), and a Diane and Guilford Glazer Foundation Faculty Fellowship (LE). We thank Dr. Eva de la Serna (Dunn lab) for culturing T-cells on EM grids and Maria Caterina Rotiroti and the Majzner lab at Stanford for providing the CAR T-cells used in this study. We thank Dr. Wah Chiu (Stanford) and Dr. Matthew J. Paszek (Cornell)for helpful discussion and Dr. Lydia-Marie Joubert for providing cryo-FIB training, experimental support, and helpful feedback. We thank the Stanford Cryo-Electron Microscopy Center (cEMc) for providing access to a Krios cryo-TEM for data collection. Cryo-FIB for this work was performed at the Stanford-SLAC CryoET Specimen Preparation Center (SCSC), which is supported by the National Institutes of Health Common Fund's Transformative High Resolution Cryoelectron Microscopy program (U24GM139166). The content is solely the responsibility of the authors and does not necessarily represent the official views of the National Institutes of Health. This manuscript was prepared using the Henriques lab bioRxiv template on Overleaf. The authors declare no competing financial interests.

## Author Contributions

LE: Conceptualization, Methodology, Validation, Investigation, Writing - Original Draft, Visualization, Supervision, Project administration. MZ: Investigation, Writing - Review & Editing. MZ: Investigation. ARD: Resources, Writing - Review & Editing, Supervision, Funding acquisition. SO: Conceptualization, Methodology, Software, Validation, Formal analysis, Investigation, Resources, Data Curation, Writing - Original Draft, Visualization, Supervision, Project administration, Funding acquisition.

## Bibliography


1. Ohad Medalia, Igor Weber, Achilleas S Frangakis, Daniela Nicastro, Günther Gerisch, and Wolfgang Baumeister. Macromolecular architecture in eukaryotic cells visualized by cryo-electron tomography. *Science*, 298(5596):1209–1213, 2002.
2. Shoh Asano, Benjamin D Engel, and Wolfgang Baumeister. In situ cryo-electron tomography: a post-reductionist approach to structural biology. *Journal of molecular biology*, 428 (2):332–343, 2016.
3. Lu Gan and Grant J Jensen. Electron tomography of cells. *Quarterly reviews of biophysics*, 45(1):27–56, 2012.
4. Saikat Chakraborty, Marion Jasnin, and Wolfgang Baumeister. Three-dimensional organization of the cytoskeleton: a cryo-electron tomography perspective. *Protein Science*, 2020.
5. Vladan Lučić, Friedrich Förster, and Wolfgang Baumeister. Structural studies by electron tomography: from cells to molecules. *Annu. Rev. Biochem.*, 74:833–865, 2005.
6. Stephan Nickell, Christine Kofler, Andrew P Leis, and Wolfgang Baumeister. A visual approach to proteomics. *Nature reviews Molecular cell biology*, 7(3):225–230, 2006.
7. Leeya Engel, Guido Gaietta, Liam P Dow, Mark F Swif, Gaspard Pardon, Niels Volkmann, William I Weis, Dorit Hanein, and Beth L Pruitt. Extracellular matrix micropatterning technology for whole cell cryogenic electron microscopy studies. *Journal of Micromechanics and Microengineering*, 29(11):115018, 2019.
8. Mauricio Toro-Nahuelpan, Ievgeniia Zagoriy, Fabrice Senger, Laurent Blanchoin, Manuel Théry, and Julia Mahamid. Tailoring cryo-electron microscopy grids by photo-micropatterning for in-cell structural studies. *Nature methods*, 17(1):50–54, 2020.
9. Léa Swistak, Anna Sartori-Rupp, Matthijn Vos, and Jost Enninga. Micropatterning of cells on em grids for efficient cryo-correlative light electron microscopy. In *Methods in Microbiology*, volume 48, pages 95–110. Elsevier, 2021.
10. Bryan S Sibert, Joseph Y Kim, Jie E Yang, and Elizabeth R Wright. Micropatterning transmission electron microscopy grids to direct cell positioning within whole-cell cryo-electron tomography workflows. *Journal of visualized experiments: JoVE*, (175), 2021.
11. Leeya Engel, Richard Held, Claudia G Vasquez, William I Weis, and Alexander R Dunn. Micropatterning em grids for cryo-electron tomography of cells. *protocols.io*, page dx.doi.org/10.17504/protocols.io.bz22p8ge, 2022.
12. Leeya Engel, Claudia G Vasquez, Elizabeth A Montabana, Belle M Sow, Marcin P Walkiewicz, William I Weis, and Alexander R Dunn. Lattice micropatterning for cryo-electron tomography studies of cell-cell contacts. *Journal of structural biology*, 213(4):107791, 2021.
13. Liam P Dow, Guido Gaietta, Yair Kaufman, Mark F Swift, Moara Lemos, Kerry Lane, Matthew Hopcroft, Armel Bezault, Cécile Sauvanet, Niels Volkmann, et al. Morphological control enables nanometer-scale dissection of cell-cell signaling complexes. *Nature Communications*, 13(1):7831, 2022.
14. Kotaro Kelley, Ashleigh M Raczkowski, Oleg Klykov, Pattana Jaroenlak, Daija Bobe, Mykhailo Kopylov, Edward T Eng, Gira Bhabha, Clinton S Potter, Bridget Carragher, et al. Waffle method: A general and flexible approach for improving throughput in fib-milling. *Nature Communications*, 13(1):1857, 2022.
15. Jane C Stinchcombe, Yukako Asano, Christopher JG Kaufman, Kristin Böhlig, Christopher J Peddie, Lucy M Collinson, André Nadler, and Gillian M Griffiths. Ectocytosis renders t cell receptor signaling self-limiting at the immune synapse. *Science*, 380(6647):818–823, 2023.
16. Hye-Ran Kim, YeVin Mun, Kyung-Sik Lee, Yoo-Jin Park, Jeong-Su Park, Jin-Hwa Park, Bu-Nam Jeon, Chang-Hyun Kim, Youngsoo Jun, Young-Min Hyun, et al. T cell microvilli constitute immunological synaptosomes that carry messages to antigen-presenting cells. *Nature Communications*, 9(1):3630, 2018.
17. Anna V Sokolova, Laurent Kreplak, Tatjana Wedig, Norbert Mücke, Dmitri I Svergun, Harald Herrmann, Ueli Aebi, and Sergei V Strelkov. Monitoring intermediate filament assembly by small-angle x-ray scattering reveals the molecular architecture of assembly intermediates. *Proceedings of the National Academy of Sciences*, 103(44):16206–16211, 2006.
18. Keyue Shen, V Kaye Thomas, Michael L Dustin, and Lance C Kam. Micropatterning of costimulatory ligands enhances cd4+ t cell function. *Proceedings of the National Academy of Sciences*, 105(22):7791–7796, 2008.
19. Zhikai Wang, Philip Moresco, Ran Yan, Jiayun Li, Ya Gao, Daniele Biasci, Min Yao, Jordan Pearson, Jaclyn F Hechtman, Tobias Janowitz, et al. Carcinomas assemble a filamentous cxcl12–keratin-19 coating that suppresses t cell–mediated immune attack. *Proceedings of the National Academy of Sciences*, 119(4):e2119463119, 2022.
20. Oluseye Ogunnigbagbe, Christopher G Bunick, and Kamaljit Kaur. Keratin 1 as a cell-surface receptor in cancer. *Biochimica et Biophysica Acta (BBA)-Reviews on Cancer*, 1877 (1):188664, 2022.
21. S Ito. Form and function of the glycocalyx on free cell surfaces. *Philosophical Transactions of the Royal Society of London. B, Biological Sciences*, 268(891):55–66, 1974.
22. Willy W Sun, Evan S Krystofiak, Alejandra Leo-Macias, Runjia Cui, Antonio Sesso, Roberto Weigert, Seham Ebrahim, and Bechara Kachar. Nanoarchitecture and dynamics of the mouse enteric glycocalyx examined by freeze-etching electron tomography and intravital microscopy. *Communications biology*, 3(1):5, 2020.
23. Koussay Dellagi and Jean-Claude Brouet. Redistribution of intermediate filaments during capping of lymphocyte surface molecules. *Nature*, 298(5871):284–286, 1982.
24. Martin J. Brown; John A. Hallam; Emma Colucci-Guyon; Stephen Shaw. Rigidity of circulating lymphocytes is primarily conferred by vimentin intermediate filaments. *J Immunol*, 166: 6640–6646, 2001.
25. Paul A Janmey, Ursula Euteneuer, Peter Traub, and Manfred Schliwa. Viscoelastic properties of vimentin compared with other filamentous biopolymer networks. *The Journal of cell biology*, 113(1):155–160, 1991.
26. Johanna Ivaska, Hanna-Mari Pallari, Jonna Nevo, and John E Eriksson. Novel functions of vimentin in cell adhesion, migration, and signaling. *Experimental cell research*, 313(10): 2050–2062, 2007.
27. Mikko Nieminen, Tiina Henttinen, Marika Merinen, Fumiko Marttila-Ichihara, John E Eriksson, and Sirpa Jalkanen. Vimentin function in lymphocyte adhesion and transcellular migration. *Nature cell biology*, 8(2):156–162, 2006.
28. Qi Da, Molly Behymer, Juliana I Correa, K Vinod Vijayan, and Miguel A Cruz. Platelet adhesion involves a novel interaction between vimentin and von willebrand factor under high shear stress. *Blood, The Journal of the American Society of Hematology*, 123(17): 2715–2721, 2014.
29. Denise Paulin, Alain Lilienbaum, Sareen Kardjian, Onnik Agbulut, and Zhenlin Li. Vimentin: Regulation and pathogenesis. *Biochimie*, 197:96–112, 2022.
30. Titilope A Fasipe, Sung-Ha Hong, Qi Da, Christian Valladolid, Matthew T Lahey, Lisa M Richards, Andrew K Dunn, Miguel A Cruz, and Sean P Marrelli. Extracellular vimentin/vwf (von willebrand factor) interaction contributes to vwf string formation and stroke pathology. *Stroke*, 49(10):2536–2540, 2018.
31. Taavi Päll, Anne Pink, Lagle Kasak, Marina Turkina, Wally Anderson, Andres Valkna, and Priit Kogerman. Soluble cd44 interacts with intermediate filament protein vimentin on endothelial cell surface. *PloS one*, 6(12):e29305, 2011.
32. Matthias Eibauer, Miriam S. Weber, Yagmur Turgay, Suganya Sivagurunathan, Robert D. Goldman, and Ohad Medalia. The molecular architecture of vimentin filaments. *bioRxiv*, 2021. doi: 10.1101/2021.07.15.452584.
33. Elizabeth Villa, Miroslava Schaffer, Jürgen M Plitzko, and Wolfgang Baumeister. Opening windows into the cell: focused-ion-beam milling for cryo-electron tomography. *Current opinion in structural biology*, 23(5):771–777, 2013.
34. Michael Marko, Chyongere Hsieh, Richard Schalek, Joachim Frank, and Carmen Mannella. Focused-ion-beam thinning of frozen-hydrated biological specimens for cryo-electron microscopy. *Nature methods*, 4(3):215–217, 2007.
35. Alexander Rigort, Felix JB Bäuerlein, Elizabeth Villa, Matthias Eibauer, Tim Laugks, Wolfgang Baumeister, and Jürgen M Plitzko. Focused ion beam micromachining of eukaryotic cells for cryoelectron tomography. *Proceedings of the National Academy of Sciences*, 109 (12):4449–4454, 2012.
36. Hao Zhu, Meijing Li, Ruixue Zhao, Ming Li, Yongping Chai, Zhiwen Zhu, Yihong Yang, Wei Li, Zhongyun Xie, Xiaomin Li, et al. In situ structure of intestinal apical surface reveals nanobristles on microvilli. *Proceedings of the National Academy of Sciences*, 119 (24):e2122249119, 2022.
37. Guillaume Le Saux, Esti Toledo-Ashkenazi, and Mark Schvartzman. Fabrication of nanoscale arrays to study the effect of ligand arrangement on inhibitory signaling in nk cells. In *The Immune Synapse: Methods and Protocols*, pages 313–325. Springer, 2023.
38. Anna Sartori-Rupp, Diégo Cordero Cervantes, Anna Pepe, Karine Gousset, Elise Delage, Simon Corroyer-Dulmont, Christine Schmitt, Jacomina Krijnse-Locker, and Chiara Zurzolo. Correlative cryo-electron microscopy reveals the structure of tnts in neuronal cells. *Nature communications*, 10(1):342, 2019.
39. Anna Pepe, Stefano Pietropaoli, Matthijn Vos, Giovanna Barba-Spaeth, and Chiara Zurzolo. Tunneling nanotubes provide a route for sars-cov-2 spreading. *Science Advances*, 8(29): eabo0171, 2022.
40. Florian Fäßler, Bettina Zens, Robert Hauschild, and Florian KM Schur. 3d printed cell culture grid holders for improved cellular specimen preparation in cryo-electron microscopy. *Journal of Structural Biology*, 212(3):107633, 2020.
41. Aidan M Tousley, Maria Caterina Rotiroti, Louai Labanieh, Lea Wenting Rysavy, Won-Ju Kim, Caleb Lareau, Elena Sotillo, Evan W Weber, Skyler P Rietberg, Guillermo Nicolas Dalton, et al. Co-opting signalling molecules enables logic-gated control of car t cells. *Nature*, pages 1–10, 2023.
42. Georg Wolff, Ronald WAL Limpens, Shawn Zheng, Eric J Snijder, David A Agard, Abraham J Koster, and Montserrat Bárcena. Mind the gap: Micro-expansion joints drastically decrease the bending of fib-milled cryo-lamellae. *Journal of structural biology*, 208(3):107389, 2019.
43. David N Mastronarde. Automated electron microscope tomography using robust prediction of specimen movements. *Journal of structural biology*, 152(1):36–51, 2005.
44. Dimitry Tegunov and Patrick Cramer. Real-time cryo-electron microscopy data preprocessing with warp. *Nature methods*, 16(11):1146–1152, 2019.
45. James R Kremer, David N Mastronarde, and J Richard McIntosh. Computer visualization of three-dimensional image data using imod. *Journal of structural biology*, 116(1):71–76, 1996.
46. Eric F Pettersen, Thomas D Goddard, Conrad C Huang, Elaine C Meng, Gregory S Couch, Tristan I Croll, John H Morris, and Thomas E Ferrin. Ucsf chimerax: Structure visualization for researchers, educators, and developers. *Protein Science*, 30(1):70–82, 2021.
47. Alessandro La Ferlita, Salvatore Alaimo, Sebastiano Di Bella, Emanuele Martorana, Georgios I Laliotis, Francesco Bertoni, Luciano Cascione, Philip N Tsichlis, Alfredo Ferro, Roberta Bosotti, et al. Rnadetector: a free user-friendly stand-alone and cloud-based system for rna-seq data analysis. *BMC bioinformatics*, 22(1):1–16, 2021.